

Shape-preserving transformation of carbonate minerals into lead-halide perovskite semiconductors based on sequential ion-exchange/insertion reactions

Tim Holtus^{1,§}, Lukas Helmbrecht^{1,§}, Hans C. Hendrikse^{1,§}, Iaroslav Baglai¹, Sophie Meuret¹, Gede W. P. Adhyaksa¹, Erik C. Garnett¹, Willem L. Noorduin^{1*}

¹AMOLF, 1098 XG Amsterdam, The Netherlands

[§]These authors contributed equally to this work.

Biological and bio-inspired mineralization processes yield a variety of three-dimensional (3D) structures with relevance for fields such as photonics, electronics, and photovoltaics. However, these processes are only compatible with specific material compositions, often carbonate salts, thereby hampering widespread applications. Here we present a strategy to convert a wide range of metal carbonate structures into lead-halide perovskite semiconductors with tunable bandgaps, while preserving the 3D shape. First, we introduce lead ions by cation exchange. Second, we use carbonate as a leaving group, facilitating anion exchange with halide, which is followed rapidly by methylammonium insertion to form the perovskite. As proof-of-principle, preprogrammed carbonate salt shapes such as vases, coral-like forms and helices are transformed into perovskites while preserving the morphology and crystallinity of the initial micro-architectures. This approach also readily converts calcium carbonate biominerals into semiconductors, furnishing biological and programmable synthetic shapes with the performance of artificial compositions such as perovskite-based semiconductors.

Strategies that offer independent control over 3D shape and composition of nano- and micro-scale architectures are of fundamental interest and hold relevance for fields ranging from optics and sensing to microelectronics and catalysis¹⁻⁹. Carbonate salts, including the most abundant biomineral calcium carbonate, give access to an impressive catalogue of exquisitely sculpted crystalline shapes that can be created via biological and bio-inspired mineralization processes with a rational control over form^{1,2,9-14}. However, these carbonate salts have limited application potential, due to the properties of their chemical composition. One way to overcome this inherent limitation is by converting previously formed shapes into a desired composition while preserving the original shape. Both biological and synthetic shapes have already been converted into functional compositions using oxidation/reduction reactions, which give access to a range of metals and metal oxides^{8,15-17}. However, many compositions that can act as conductors, semiconductors and catalysts cannot be synthesized using these reactions. An entirely different and potentially more versatile approach to tune the material composition by choice is offered by ion-exchange reactions. These reactions enable the conversion of the ionic composition of nanocrystals—and superlattices thereof—into a wide range of

compositions, whilst preserving the original morphology¹⁸⁻²⁸. Cation exchange has already been demonstrated for many different ions²⁰. Anion exchange, on the contrary, remains challenging as the larger size and lower diffusivity of anions hinder proper conversions. As a result, only a few examples of successful anion exchange reactions have been reported^{23,24}, and general routes to exchange anions still need to be developed. Here we demonstrate a versatile pathway towards complete cationic and anionic exchange with full shape preservation, starting from a variety of biological and bio-inspired artificial structures. Two key insights underlie this approach. Firstly, the anionic carbonate group in biological and bio-inspired minerals can act as a remarkably good leaving group, offering a promising way to introduce new anions in a relatively facile and generic manner. Secondly, many biomineralized architectures are composed of nanocomposites, i.e., materials composed of an ensemble of nanocrystals embedded in an amorphous matrix, and this nanocrystalline nature may readily enable the tuning of their composition using ion-exchange reactions. This applies not only to biologically formed structures, but also to the rich variety of synthetic bioinspired materials, for which numerous strategies exist to yield rationally designed shape-controlled hybrid materials^{2-5,9-14}. Exploiting these two unique advantages will thus enable the possibility to first program the shape in a carbonate salt nanocomposite and subsequently apply a cascade of cation and anion conversion reactions to obtain a functional-material composition, e.g. a semiconductor or catalyst, of the exact same shape.

To demonstrate the proof-of-principle we chose methylammonium lead-halide perovskites ($\text{CH}_3\text{NH}_3\text{PbX}_3$) as target materials. The exceptional performance of these semiconductors for solar cells, water-splitting, lasers, LEDs and radiation detectors along with their facile synthesis is revolutionizing the prospects of next-generation optoelectronics²⁹. So far most studies have been performed on thin films, but control over the 3D microscale morphology of perovskites may be essential for developing the next generation of transistors and directed light-absorption and emission³⁰. Despite the recent progress in casting methods^{31,32}, growth of arbitrary perovskite shapes has remained challenging, and highlights the need for new strategies to gain independent control over shape and composition.

In this work we introduce a simple two-step reaction scheme for converting carbonate architectures into lead-halide perovskites (Fig. 1). Starting from biological and programmable synthetic carbonate-salt architectures we convert these into perovskites with a tunable bandgap and a charge carrier lifetime on par with state-of-the-art perovskite thin films, while at the same time inheriting the 3D shape, fine features, and crystallinity of the starting architecture.

Results and discussion

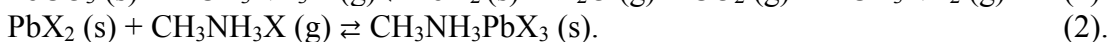
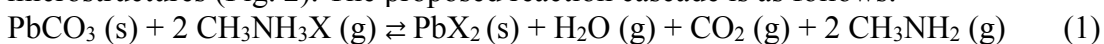
Conversion of carbonate salts into perovskites requires a complete chemical and structural transformation involving the exchange of the cations and the notoriously difficult exchange of anions, insertion of methylammonium halide ($\text{CH}_3\text{NH}_3\text{X}$), and rearrangement of the crystal unit cell, while in all steps minimizing the distortion of the crystal lattices (Fig. 1). A key insight for the development of our route is that PbX_2 , a commonly used precursor for synthesizing lead halide perovskites^{33,34}, crystallizes in the

same orthorhombic crystal structure as PbCO_3 (cerussite) and many other carbonate salts MCO_3 (with $\text{M} = \text{i.e. Ba, Sr, or Ca}$ in the witherite, strontianite, and aragonite crystal structures, respectively). More explicitly, the metal ions in the crystal structures of PbX_2 , PbCO_3 and MCO_3 are in the same position, and the dimensions of the unit cells are closely matched, with the length of the unit cell axes changing typically less than 10%. Additionally, the carbonate group can act as a good leaving group for facilitating the insertion of the halides into the PbCO_3 structure. Our two-step reaction scheme thus allows us to synthesize lead-halide perovskites from arbitrarily chosen metal carbonate architectures by first exchanging the metal ions for lead, followed by the reaction of the carbonate ions with methylammonium halides to directly yield the corresponding perovskite.

Prior to performing the conversion reaction, we program the carbonate shape into the desired target structure. For the proof-of-principle, we use the bio-inspired coprecipitation of barium and strontium carbonate nanocrystals with silica. This nanocomposite system offers a pragmatic platform for developing a wide selection of micro-sized 3D geometries including vase, spiral, and coral shapes, which can be formed by rationally modulating the reaction conditions such as temperature, pH and CO_2 concentration^{9,13,14}. We illustrate the concept of the conversion reactions on coral-like shapes of barium carbonate and silica ($\text{BaCO}_3/\text{SiO}_2$) (Fig. 2a, see Supplementary Information SI for details).

In the first step we exchange the Ba^{2+} for Pb^{2+} while preserving the shape of the original microstructure (Fig. 2). During this exchange reaction it is essential to prevent the dissolution of BaCO_3 and subsequent nucleation of PbCO_3 , as such dissolution/recrystallization process hinders a preservation of the shape³⁵. Since the dissolution/recrystallization is relatively slow for high concentrations of Pb^{2+} , we perform the reaction in a nearly saturated aqueous solution of 0.9 M $\text{Pb}(\text{NO}_3)_2$ for 30-60 seconds in the absence of CO_2 . This reaction is rapidly driven to completion due to the high concentration of Pb^{2+} and because the thermodynamic stability of the resulting PbCO_3 is higher, as indicated by the solubility product of PbCO_3 ($K_{\text{sp}} = 7.4 \cdot 10^{-14}$), which is orders of magnitude lower than that of BaCO_3 ($K_{\text{sp}} = 2.58 \cdot 10^{-9}$)^{22,36}. Additionally, the similarities between the orthorhombic crystals structures of both BaCO_3 and PbCO_3 minimize distortion of the unit cell during the conversion. Energy Dispersive X-ray Spectroscopy (EDS) confirms the virtually complete exchange from Ba^{2+} to Pb^{2+} throughout the interior of the structure (>98 at.%, Fig. 2, SI). As expected, the orthorhombic crystal structure is maintained during the conversion of BaCO_3 into PbCO_3 , which can be concluded from the nearly identical X-Ray powder diffraction (XRPD) data. Scanning Electron Microscopy (SEM) reveals the preservation of the entire architecture with nanoscale fidelity, while even the initial crystallographic alignment along the c -axis of the nanocrystals is retained according to the Maltese cross birefringent pattern of both the BaCO_3 and PbCO_3 using polarization microscopy (Supplementary Fig. 4)¹³. This preservation of nanoscale features and crystallographic orientation suggests a transformation in which a single crystal of one phase transforms into a single crystal of a different phase while inheriting its orientation from the original crystal, thus constituting an additional level of complexity over dissolution/recrystallization mechanisms.

In the second step we convert the resulting PbCO_3 architectures directly into the desired $\text{CH}_3\text{NH}_3\text{PbX}_3$ perovskite. The required exchange of anions has remained challenging in other systems thus far, since the larger size and lower diffusivity of anions often leads to sluggish conversions and poor retention of the morphology²⁰. Besides replacing the carbonate with a desired halide-anion X (X = Cl, Br or I), the reaction to perovskite requires the well-established insertion of $\text{CH}_3\text{NH}_3\text{X}$ and rearranging the crystal structure to yield the perovskite³³. We here address these challenges in a one-pot conversion by exposing the PbCO_3 architectures to an excess of gaseous $\text{CH}_3\text{NH}_3\text{X}$ at 120°C for ca. 6 hours, which results in the direct formation of the desired perovskite ($\text{CH}_3\text{NH}_3\text{PbX}_3$). Characterization of the resulting structures shows excellent conversion of PbCO_3 into the desired perovskite while retaining both the shape and fine features of the starting microstructures (Fig. 2). The proposed reaction cascade is as follows:



In the first step, the removal of H_2O , CO_2 and CH_3NH_2 from the reaction mixture drives the reaction to completion, which is consistent with Le Chatelier's principle. Additionally, the removal of water prevents the undesired decomposition of the perovskite, although small concentrations of water may improve the quality of the perovskite by lowering the defect density³⁷⁻³⁹. In the second step, the excess amount of $\text{CH}_3\text{NH}_3\text{X}$ pushes the reaction of the intermediate PbX_2 to the perovskite.

To confirm the proposed reaction mechanism, we first develop a method for methylamine CH_3NH_2 detection. For this we use a UV-light absorbing aromatic aldehyde that reacts with methylamine to form an imine that can be detected by HPLC-UV (High performance liquid chromatograph coupled to an UV-detector, see SI for details). This analysis shows that methylamine is released during the conversion of PbCO_3 to the perovskite, in agreement with the first step of the proposed mechanism. Consistent with this mechanism, we can also gain direct access to the PbX_2 intermediate by reacting PbCO_3 microstructures with KI under acidic conditions to obtain the corresponding PbI_2 microstructures (SI). In the second step $\text{CH}_3\text{NH}_3\text{X}$ is inserted into PbX_2 to form $\text{CH}_3\text{NH}_3\text{PbX}_3$. This reaction is already well documented for pure PbX_2 crystals³³. Using the microstructures of PbI_2 we also confirm that the microstructures can undergo this insertion reaction with $\text{CH}_3\text{NH}_3\text{I}$ to form the corresponding $\text{CH}_3\text{NH}_3\text{PbI}_3$ structure. Finally, we qualitatively investigate the relative reaction rates of the two consecutive reaction steps by partially reacting PbCO_3 structures to $\text{CH}_3\text{NH}_3\text{PbX}_3$ according to the one-pot conversion scheme. Analysis of these structures using XRD show no detectable amounts of the reaction intermediate PbX_2 , suggesting that the anion exchange of PbCO_3 to PbX_2 (step 1) is relatively slow compared to the conversion of PbX_2 to $\text{CH}_3\text{NH}_3\text{PbX}_3$ (step 2).

The generality of our reaction scheme allows us to synthesize a range of perovskites starting from a wide choice of carbonate compounds. To demonstrate this we successfully convert microstructures of BaCO_3 , SrCO_3 and CaCO_3 into the corresponding chloride, bromide and iodide perovskites (Fig. 2b, c, and SI). It should be noted that the silica (20-25 at.% of the entire composition) is inert during the entire sequence of

conversions, and merely required for controlling the shape of the original MCO_3 structure before we start with the conversions^{9,13,14}. However, during the conversions the silica matrix can assist in stabilizing and maintaining the overall micro shape by acting as a scaffold and by hindering ripening of the nanocrystals.

In order to verify the quality of our 3D shaped perovskites and the potential for our approach in optoelectronic applications, we benchmark the photoluminescence (PL) spectra and PL lifetime of our 3D halide-perovskite microstructures against already reported standard thin-film perovskites. Our 3D perovskites show narrow PL emission, with the peak wavelength tunable from the blue into the near-infrared by selecting the methylammonium halide precursor (Fig. 3a), comparable to what has been reported in literature for thin-film perovskites³⁴. The photoluminescence lifetime of 28 ns for $\text{CH}_3\text{NH}_3\text{PbBr}_3$ microstructures is also on par with standard material preparation methods of thin films (Fig. 3b)³⁴. We also see excellent PL uniformity both within and across large fields of halide-perovskite microstructures, confirming the complete conversion of the samples (Fig. 3c). Our perovskites thus perform comparable to state-of-the-art thin film perovskites, while offering the ability to straightforwardly program the 3D shape.

Since our conversion process is to a large extent independent of the microscopic form of the mineralized architecture, a wide variety of perovskite shapes can be synthesized by first programming the shape of the starting carbonate structures and subsequently converting them into lead-halide perovskite materials^{9,14}. To illustrate the versatility of our concept, we preprogram different morphologies by modulating the reaction conditions such as pH, temperature and CO_2 concentration during the co-precipitation process of carbonate and silica (see SI for details). Subsequently, these structures can be converted to perovskites with a tunable bandgap based on the choice of methylammonium halide precursor. The photoluminescence can be seen with great spatial resolution in the cathodoluminescence (CL) images of a selection of perovskite spirals, trumpets, spiked corals, and vases (Figure 4).

The colors of the CL images in Figure 4A-E correspond to the real color of light emitted from the perovskite microstructures (peak wavelength), showing the tunability of the bandgap by selecting the methylammonium halide precursor. Our reaction scheme thus enables the synthesis of a wide repertoire of programmable 3D perovskites with independent control over the micro-shape and material composition.

Our simple and flexible conversion approach also applies to naturally occurring biomineral structures made of CaCO_3 , many of which have a comparable nanocrystalline layout and material composition to the artificially synthesized carbonate shapes¹⁰⁻¹². We illustrate this concept by converting a 6x15x3 mm section of the highly intricate aragonite architecture of a cuttlefish bone (from *Sepia officinalis*) into perovskite, while retaining even the fine structure of the sub-micrometer-thin lamella (Fig. 4f, for larger samples see SI). The epitaxial relationship between aragonite and the most common CaCO_3 polymorph, calcite, suggests that these biominerals can be converted as well. We confirm this by converting a 3.5 cm sized calcite shell of a sand dollar (*Mellita isometra*) into $\text{CH}_3\text{NH}_3\text{PbBr}_3$. To speed up the reaction rate due to the slow mass transport in the

gas phase reaction, we perform the conversion of PbCO_3 into perovskite in a solution containing the methylammonium halide precursor instead of the gas-phase reaction. Even though a low pH can deteriorate perovskites, we here use acidic conditions to turn the carbonate of PbCO_3 into a good leaving group and speed up the conversion reaction. To directly visualize the transformation, we use UV illumination to observe the light emission from the forming perovskite. The reaction is remarkably fast, with a 3.5 cm sand dollar converting in less than one minute, as is clearly visible from the bright fluorescent true-color camera images (Fig. 4g) and the full movie of the process in the SI (Movie 1). This experiment also gives insight in the conversion depth that can be achieved: for a sand dollar with a thickness of ca. 1 mm, we find that the outer 100 μm is converted into perovskite, giving rise to a core-shell structure with a semiconductor on the outside and an insulating CaCO_3 interior (Supplementary Fig. 3). Thus, our transformation scheme is also effective on macroscopic scales, yet preserves even the finest features with sub-micrometer fidelity.

Conclusions

In summary, we present a platform to gain independent control over both shape and composition of 3D functional materials, using a two-step reaction scheme that converts biological and programmable synthetic carbonate-salt architectures into perovskites. With calcium carbonate being the most abundant biomineral in nature, our reaction thus gives access to the vast catalogue of biological architectures, leveraging nature's exquisite morphogenesis strategies with chemical conversion into broadly applicable functional materials^{1-5,7-16,40}. Furthermore, the control offered by bio-inspired synthetic crystallization strategies over parameters such as nucleation position, shape, and crystal size can now be combined with the unprecedented material performance of artificially-made halide perovskites with tunable optical and electronic properties. Finally, these principles can readily be extended to the synthesis of other functional materials, potentially including other semiconductors such as lead-free perovskites, conductors and catalysts.

Methods

Details are available in the Supplementary Information.

Growth of BaCO_3 microstructures. An aluminum plate (2x2 cm) was placed vertically in a 100 mL beaker containing 74 mg BaCl_2 and 16 mg Na_2SiO_3 in 15 mL of water. The plate was placed in such a way that it was partly submerged and the meniscus of the solution ran along its surface. The beaker was covered with a petri dish to allow CO_2 from the air to slowly diffuse into the reaction mixture. After 1.5-2.0 hours, the growth was halted by removing the aluminum plate from the solution and carefully washing it with deionized water (see also SI section 1). The resulting structures were analyzed using XRD (SI section 7), SEM/EDS (SI section 8) and Optical Microscopy (SI section 9).

Conversion of BaCO_3 microstructures to PbCO_3 . BaCO_3 microstructures prepared by the above mentioned method were placed directly after growth in an airtight jar containing 15 g of $\text{Pb}(\text{NO}_3)_2$ in 50 mL of degassed water. This degassed water was prepared by bubbling nitrogen through it for 1 hour prior to the conversion reaction. Furthermore nitrogen was flowed through the airtight jar while the $\text{Pb}(\text{NO}_3)_2$ was dissolving in it to ensure no additional CO_2 was present in the solution. The

microstructures were fully submerged for 30-60 seconds to allow full conversion to take place, and were afterwards washed with deionized water and acetone (see also SI section 2). The resulting structures were analyzed with the same methods as the BaCO₃ microstructures.

Conversion of PbCO₃ microstructures to CH₃NH₃PbX₃. PbCO₃ microstructures were placed in the middle of a single zone horizontal tube furnace. Subsequently an alumina boat containing methyl ammonium halide (chlorine, bromine or iodine) was inserted into the tube and placed in the cold zone just outside the oven. The tube was purged of oxygen by lowering the pressure to below 0.1 mbar and flushing the system with argon. This process was repeated three times and afterwards the pressure was lowered to 70 mbar while maintaining a 30 sccm flow of argon. The temperature of the furnace was raised to 120 °C and the alumina boat was moved right next to the sample slide inside the furnace. After 6 hours the reaction was stopped by switching off the oven and allowing it to cool to room temperature while at the same time increasing the pressure inside the tube to atmospheric conditions. (see also SI section 3). The resulting structures were analyzed with XRD (SI section 7), SEM/EDS (SI section 8), Photoluminescence (SI section 10 and 12) and Cathodeluminescence (SI section 11).

Data availability. The data that support the findings of this study are provided within the article and in the Supplementary Information or can be obtained from the corresponding author on request.

References

1. Fratzl, P. Biomimetic materials research: what can we really learn from nature's structural materials. *J. R. Soc. Interface* **4**, 637-642 (2007).
2. Nudelman, F. & Sommerdijk, N. A. J. M. Biomineralization as an inspiration for materials chemistry. *Angew. Chem. Int. Ed.* **21**, 6582-6596 (2012).
3. Studart, A. R. Towards high-performance bioinspired composites. *Adv. Mater.* **24**, 5024-5044 (2012).
4. Wegst, U. G. K., Bai, H., Saiz, E., Tomsia, A. P. & Ritchie, R. O. Bioinspired structural materials. *Nat. Mater.* **14**, 23-36 (2014).
5. Di Giosia, M. *et al.* Bioinspired nanocomposites: ordered 2D materials within a 3D lattice. *Adv. Funct. Mater.* **26**, 5569-5575 (2016).
6. Xu, S. *et al.* Assembly of micro/nanomaterials into complex, three-dimensional architectures by compressive buckling. *Science* **347**, 154-159 (2015).
7. Nie, Z., Petukhova, A. & Kumacheva, E. Properties and emerging applications of self-assembled structures made from inorganic nanoparticles. *Nat. Nanotech.* **5**, 15-25 (2010).
8. Bao, Z. *et al.* Chemical reduction of three-dimensional silica micro-assemblies into microporous silicon replicas. *Nature* **446**, 172-175 (2007).
9. Kaplan, C. N. *et al.* Controlled growth and form of precipitating microstructures. *Science* **355**, 1395-1399 (2017).
10. Lowenstam, H. A. & Weiner, S. *On Biomineralization*. (Oxford University Press, Oxford, UK, 1989).
11. Mann, S. *Biomineralization*. (Oxford University Press, Oxford, UK, 2002).

12. Mann, S. & Ozin, G. A. Synthesis of inorganic materials with complex form. *Nature* **382**, 313-318 (1996).
13. García-Ruiz, J. M., Melero-García, E. & Hyde, S. T. Morphogenesis of self-assembled nanocrystalline materials of barium carbonate and silica. *Science* **323**, 362-365 (2009).
14. Noorduin, W. L., Grinthal, A., Mahadevan, L. & Aizenberg, J. Rationally designed complex, hierarchical microarchitectures. *Science* **340**, 832-837 (2013).
15. Sandhage, K. H. *et al.* Novel, bioclastic route to self-assembled 3D, chemically tailored meso/nanostructures: shape-preserving reactive conversion of biosilica (diatom) microshells. *Adv. Mater.* **14**, 429-433 (2002).
16. Weatherspoon, M. R., Allan, S. M., Hunt, E., Cai, Y. & Sandhage, K. H. Sol-gel synthesis on self-replicating single-cell scaffolds: applying complex chemistries to nature's nanostructured templates. *Chem. Commun.* 651-653 (2005).
17. Wu, H., *et al.* Electrospun metal nanofiber webs as high-performance transparent electrodes. *Nano Lett.* **10**, 4242-4248 (2010).
18. Son, D. H., Hughes, S.M., Yin, Y. & Alivisatos, A. P. Cation exchange reactions in ionic nanocrystals. *Science* **306**, 1009-1012 (2004).
19. Robinson, R. D. *et al.* Spontaneous superlattice formation in nanorods through partial cation exchange. *Science* **317**, 355-358 (2007).
20. Beberwyck, B. J., Surendranath, Y. & Alivisatos, A. P. Cation exchange: a versatile tool for nanomaterials synthesis. *J. Phys. Chem. C* **117**, 19759-19770 (2013).
21. Putnis, A. Mineral replacement reactions: from macroscopic observations to microscopic mechanisms. *Mineral. Mag.* **66**, 689-708 (2002).
22. De Trizio, L. & Manna, L. Forging colloidal nanostructures via cation exchange reactions. *Chem. Rev.* **116**, 10852-10887 (2016).
23. Hodges, J. H., Kletetschka, K., Fenton, J. L., Read, C. G. & Schaak, R. E. Sequential anion and cation exchange reactions for complete material transformations of nanoparticles with morphological retention. *Angew. Chem. Int. Ed.* **54**, 8669-8672 (2015).
24. Wu, H.-L. *et al.* Formation of pseudomorphic nanocages from Cu₂O nanocrystals through anion exchange reactions. *Science* **351**, 1306-1310 (2016).
25. Stebe, K. J., Lewandowski, E. & Ghosh, M. Oriented assembly of metamaterials. *Science* **325**, 159-160 (2009).
26. Boneschanscher, M. P. *et al.* Long-range orientation and atomic attachment of nanocrystals in 2D honeycomb superlattices. *Science* **344**, 1377-1380 (2014).
27. Geuchies, J. *et al.* In situ study of the formation mechanism of two-dimensional superlattices from PbSe nanocrystals. *Nat. Mater.* **15**, 1248-1254 (2016).
28. Miszta, K. *et al.* Hierarchical self-assembly of suspended branched colloidal nanocrystals into superlattice structures. *Nat. Mat.* **10**, 872-876 (2011).
29. Zhang, W., Eperon, G. E. & Snaith H. J. Metal halide perovskites for energy applications *Nat. Energy*, **1**, 16048-16056 (2016).
30. Polman, A., Atwater, H. A. Photonic design principles for ultrahigh-efficiency photovoltaics. *Nat. Mater.* **11**, 174-177 (2012).
31. Chen, K. & Tüysüz, H. Morphology-controlled synthesis of organometal halide perovskite inverse opals. *Angew. Chem. Int. Ed.* **54**, 13806-13810 (2015).

32. Ashley, M. J. *et al.* Templated synthesis of uniform perovskite nanowire arrays. *J. Amer. Chem. Soc.* **138**, 10096–10099 (2016).
33. Burschka, J. *et al.* Sequential deposition as a route to high-performance perovskite-sensitized solar cells. *Nature* **499**, 316-319 (2013).
34. Sheng, R. *et al.* Methylammonium lead bromide perovskite-based solar cells by vapor-assisted deposition. *J. Phys. Chem. C* **119**, 3545-3549 (2015).
35. Yuan, K., Lee, S. S., De Andrade, V., Sturchio, N. C. & Fenter, P. Replacement of calcite (CaCO₃) by cerussite (PbCO₃). *Environ. Sci. Technol.* **50**, 12984-12991 (2016).
36. North Carolina State University database for solubility constants: http://www4.ncsu.edu/~franzen/public_html/CH201/data/Solubility_Product_Constants.pdf.
37. Niu, G. Li, W., Meng, F., Wang, L., Dong, H., Qui, Y. Study on stability of CH₃NH₃PbI₃ films and effect of post modification by aluminum oxide in all-solid-state hybrid solar cell. *J. Mater. Chem. A.* **2**, 705-711 (2014).
38. Tenuta E., Zheng, C. & Rubel, O. Thermodynamic origin of instability in hybrid halide perovskites. *Sci. Rep.* **6**, 1-8 (2016).
39. Eperon, G. E. *et al.* The importance of moisture in hybrid lead halide perovskite thin film fabrication. *ACS Nano*, **9**, 9380-9393 (2015).
40. Li, L, Fijneman, A. J., Kaandorp, J. A., Aizenberg, J., Noorduin, W. L. Directed nucleation and growth by balancing local supersaturation and substrate/nucleus lattice mismatch. *Proc. Natl. Acad. Sci.* (in press) (2018).

Acknowledgements

The authors thank T. Coenen for assistance with the CL measurements, S. Britzman for technical help and discussions, L. M. C. Janssen for help with the manuscript and J. C. Weaver for identification of the biominerals. W.L.N. thanks the Netherlands Organization for Scientific Research (NWO) for financial support from a VENI grant. E.C.G. was partially supported by the European Research Council under the European Union's Seventh Framework Programme (FP/2007-2013)/ERC grant agreement no. 337328, 'NanoEnabledPV' and by an STW VIDI grant. S.M. acknowledges funding from the European Research Council (grant agreement no. 695343). Scanning electron microscopy was performed at the fabrication and characterization facilities of the Amsterdam nanoCenter, supported by NWO.

Author contributions

T.H., L.H., and H.C.H. contributed equally to this work. E.C.G. and W.L.N. conceived the initial idea. T.H., L.H., and H.C.H. designed, performed, and analyzed the experiments. I.B. designed and performed the methylamine detection, S.M. performed the CL analysis, and G.W.P.A. performed the PL lifetime measurement. W.L.N. wrote the manuscript with the input of all the other authors.

Additional information

Supplementary information is available in the online version of the paper. Reprints and permissions information is available online at www.nature.com/reprints. Publisher's note: Springer Nature remains neutral with regard to jurisdictional claims in published maps and institutional affiliations. Correspondence and requests for materials should be addressed to W.L.N.

Competing financial interests

The authors declare no competing financial interests.

Figures

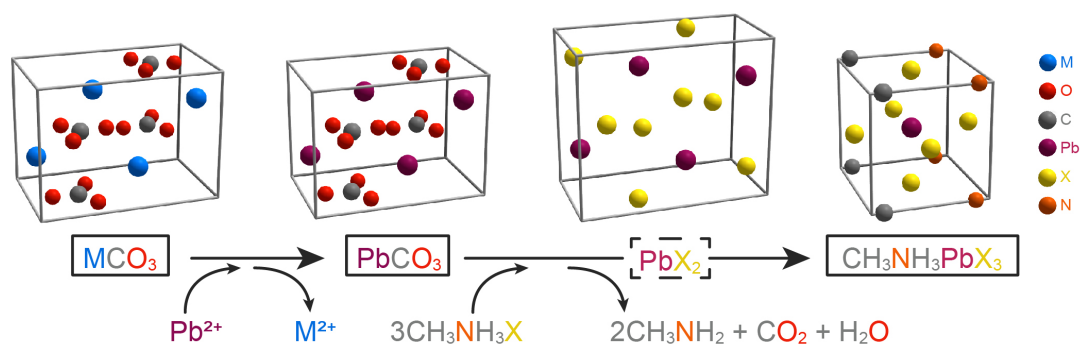


Figure 1. Reaction scheme for the synthesis of $\text{CH}_3\text{NH}_3\text{PbX}_3$ perovskites from carbonate salts MCO_3 , M (blue) = Ca, Ba or Sr, X (yellow) = Cl, Br or I, Pb (purple), O (red), N (orange), C and H (both grey). The reaction of PbCO_3 with $\text{CH}_3\text{NH}_3\text{X}$ results in the direct formation of $\text{CH}_3\text{NH}_3\text{PbX}_3$ via the intermediate PbX_2 (dashed box). The cation organization in the crystal unit cell of the carbonate salts and PbX_2 is similar, thereby facilitating the cation exchange reaction. The sizes of the unit cells are scaled for the conversion of BaCO_3 to $\text{CH}_3\text{NH}_3\text{PbBr}_3$.

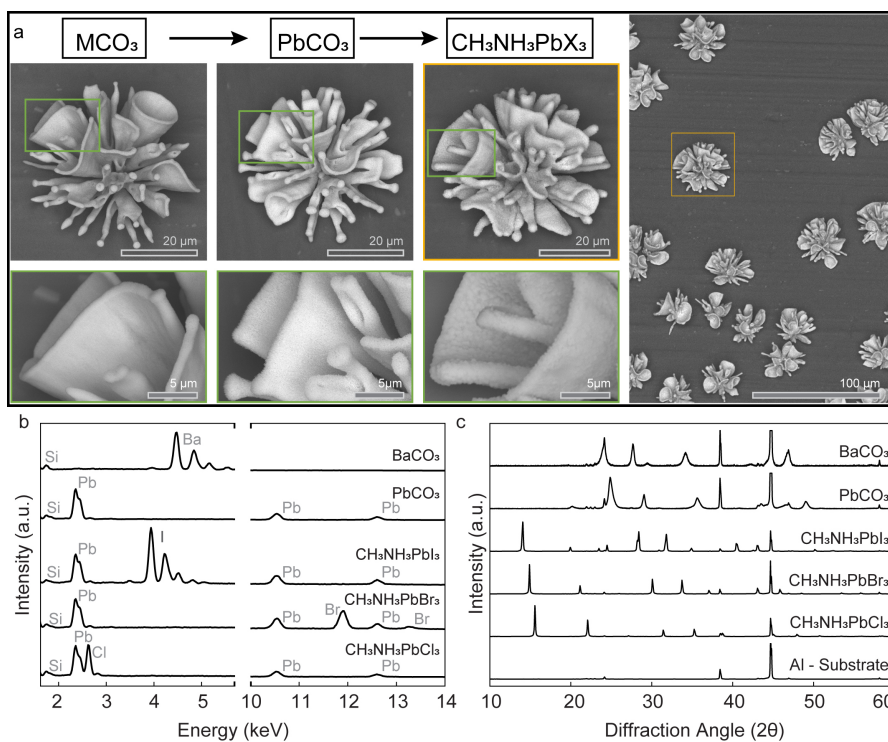


Figure 2. Conversion of metal carbonate microstructures into $CH_3NH_3PbX_3$ perovskites. **a**, Scanning electron micrographs from the sequential reaction products and overview images of the final perovskite product, shown for the conversion of $BaCO_3$ into $CH_3NH_3PbBr_3$ (see SI for details and SEM images of the $CH_3NH_3PbI_3$ and $CH_3NH_3PbCl_3$ structures). **b**, Energy dispersion spectroscopy of microstructures data showing the conversion of $BaCO_3$ into $PbCO_3$ and the final product $CH_3NH_3PbX_3$. **c**, X-Ray powder diffraction data of microstructures showing the conversion of $BaCO_3$ (witherite) into $PbCO_3$ (cerussite) and the final product $CH_3NH_3PbX_3$.

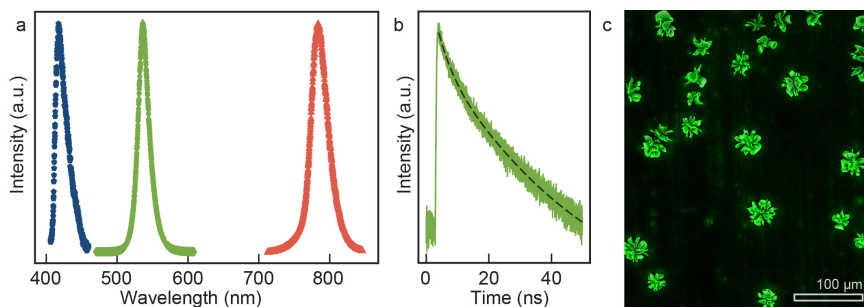


Figure 3. Photoluminescence of perovskite microstructures. **a**, PL of coral-shaped synthetic microstructures of lead halide perovskites $CH_3NH_3PbX_3$, $X=Cl$ (blue graph), Br (green graph), and I (red graph) measured with an excitation wavelength of 365 nm, 405 nm and 532 nm respectively. **b**, PL lifetime of a $CH_3NH_3PbBr_3$ microstructure. **c**, Overlay image of SEM and corresponding fluorescence microscopy image of a field of $CH_3NH_3PbBr_3$ coral shapes.

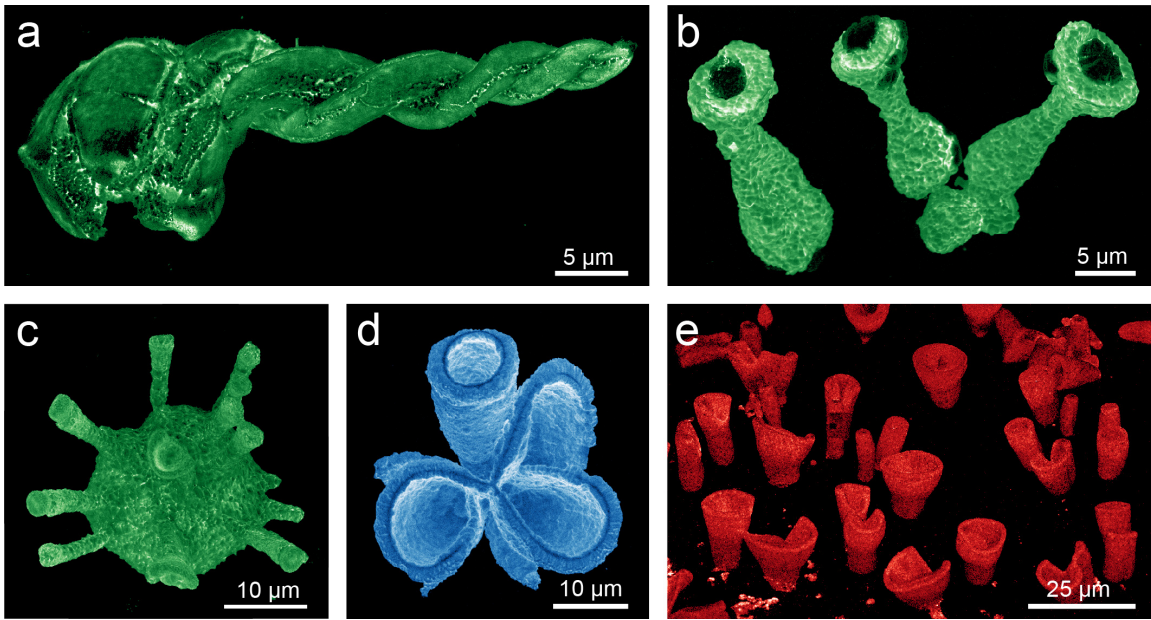


Figure 4. Complex arbitrary shaped perovskites from synthetic and biological mineral architectures. a, Spiral, b, trumpet, and c, spiked-coral shapes of $\text{CH}_3\text{NH}_3\text{PbBr}_3$. d, $\text{CH}_3\text{NH}_3\text{PbCl}_3$ coral shape. e, Field of $\text{CH}_3\text{NH}_3\text{PbI}_3$ vase shapes. The color chosen for the color scale is selected to represent the emission range measured in CL, lighter colors correspond to higher emission. f, Fluorescence microscopy image of a cuttlefish bone converted into $\text{CH}_3\text{NH}_3\text{PbBr}_3$ (inset photograph under daylight illumination, image width 0.5 cm). g, Time-lapse fluorescence photographs under UV illumination at 365 nm of a sand dollar converting in 45 seconds from PbCO_3 into $\text{CH}_3\text{NH}_3\text{PbBr}_3$.